Elastic-Actuation Mechanism for Repetitive Hopping Based on Power Modulation and Cyclic Trajectory Generation

Won Dong Shin [ID], William Stewart [ID], *Member, IEEE*, Matt A. Estrada [ID], *Member, IEEE*,
Auke J. Ijspeert [ID], *Fellow, IEEE*, and Dario Floreano [ID], *Senior Member, IEEE*

Abstract—**Animal locomotion results from a combination of power modulation and cyclic appendage trajectories, but combining these two properties in small-sized robots is difficult. Here, we introduce and characterize a new elastic actuation system based on an inverted cam that is capable of generating cyclic locomotion with controlled elastic energy charge and release for small-sized robots. We designed a leg linkage and attached to the inverted cam to develop a single legged hopping platform with one actuated degree of freedom. The hopping platform was able to continuously hop forward at 1.82 Hz. The average horizontal hopping distance was 18.7 cm, and the average forward speed was 0.34 m/s. This speed was corresponding to a Froude number of 0.14. The energy consumed for one hop was 2.09 J, and the corresponding energetic cost of transport was 6.43. The combination of inverted cam and cyclic trajectory generation has the potential to be used in other robotic applications, such as flapping wings in the air and tail fin waving in water.**

Index Terms—**Elastic actuation, legged robots, mechanism design, underactuated robots.**

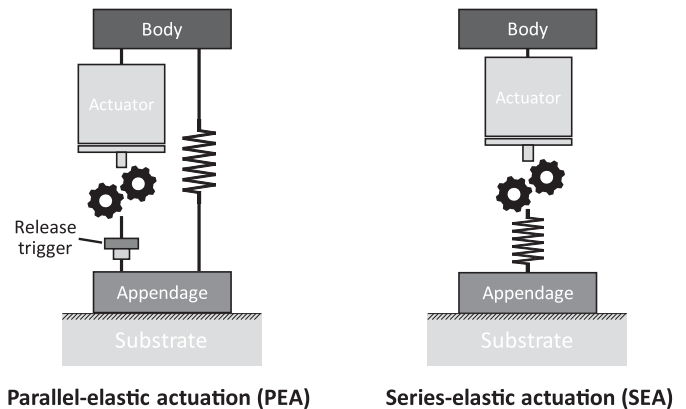**Parallel-elastic actuation (PEA)**   **Series-elastic actuation (SEA)**

Fig. 1. PEA and SEA. PEA connects the body and the leg with the actuator and elastic element in parallel. This structure allows the actuator to store elastic energy in the elastic element until a physical release trigger is activated. SEA connects the actuator and the elastic element in series. The elastic element in SEA stores energy when the appendage have contact with an environment. Both systems may have a gear box to increase the output torque with reduced operating speed.

I. INTRODUCTION

ANIMALS often achieve continuous dynamic locomotion, such as hopping [1], wing flapping [2], [3], and tail wagging [4], [5] by means of a combination of power modulation and cyclic appendage trajectories [6], [7]. Power modulation is a strategy in which the animal stores energy in its tendons over a short time before releasing it all at once for explosive movement [8]–[13]. Cyclic trajectory allows the animal to have continuous locomotion and seamless transition between energy storing and releasing phases during the locomotion [10]. In this article, cyclic trajectory refers to a continuous trajectory that is repeatedly traveled in one direction. Properly combining power modulation and cyclic movements in relatively small-sized legged robots is difficult. Although there have been many efforts to apply power modulation to relatively small-sized robotic platforms [14]–[33], to the best of authors' knowledge, all of them had limitations either in generating cyclic appendage trajectories or in storing elastic energy due to uncontrolled energy charge and release.

The weights of the cited small-sized platforms range from 1.1 g [24] to 1.3 kg [26]. Generally, legged robots heavier than 1.3 kg combine power modulation and cyclic appendage trajectories with multiple actuators [34]–[37]. The increased number of actuators increases power output and degrees of freedom, but it also increases the weight of the platform. The increased weight then requires the actuators to be more powerful and heavier to support the increased weight [38]. This phenomenon is more significant in small-scaled robots, thus increasing number of actuators is not an ideal solution to provide power modulation

and cyclic appendage trajectory for small-scaled robots. Here, our goal is to combine both in a system with a single actuator.

Power modulation has been recreated in small-scaled robotic platforms through the use of elastic actuation systems [14]–[30], [32], [33]. These systems are comprised of an elastic element and an actuator. The single actuator strategy keeps weight down in systems equipped with elastic actuation. The application of elastic actuation systems is particularly widespread in robotic hoppers because hopping requires lightweight and instantaneous high power output to push a body off the ground. There are two types of elastic actuation systems: parallel-elastic actuation (PEA) and series-elastic actuation (SEA) [39]–[41] (see Fig. 1).

The PEA used in the hopping platforms couples an actuator and an elastic element in parallel. The actuator continuously provides energy to be stored in the elastic element. At a given stored energy level, a passive trigger is activated. At this point, the actuator and the elastic element are no longer in contact, and the elastic element releases the stored energy. This controlled energy storing and releasing strategy allows PEA to increase the elastic energy capacity by using stiffer elastic element and adjusting the trigger activation timing. However, the parallel structure between the actuator and the elastic element requires a rigid connection between the elastic element and the fixed structure of the robot. This prevents PEA systems from generating a cyclic trajectory and instead limits them to oscillatory motion. In this article, oscillatory motion refers to following a trajectory with back and forth motion created by changing the direction at each tip of the trajectory as opposed to cyclic motion, which corresponds to a closed trajectory without reversal of direction.

The EPFL jumper [14] is an example of a hopper equipped with PEA. The EPFL jumper used an eccentric cam to store elastic energy in a torsion spring. The robot was capable of storing elastic energy into the torsion spring and releasing it when the cam radius reached its maximum. With the controlled energy storage and release, the EPFL jumper could jump vertically 138 cm (27 times its body size). However, the parallel structure hindered EPFL jumper from using a cyclic trajectory. Since the torsion spring was fixed to the body, the tip of the leg connected to the torsion spring could only generate an oscillating arc-shaped trajectory due to the limited range of the spring. Also, energy storing and releasing generated opposite foot trajectory directions along the arc-shaped trajectory. As a result, the robot was stationary on the ground while storing energy because the body movement direction was opposite to the take-off direction.

On the other hand, SEA couples an actuator and an elastic element in series. This series connection allows the appendage to change its position as the actuator runs without constraint from the elastic element [40]. Thus, the appendage attached to the elastic element is capable of generating a cyclic trajectory. However, the series connection means that the energetic state of the elastic element is not directly controlled by the actuator, but rather by an external force. As a result, SEA generally provides limited elastic energy and peak power [42] due to premature energy release.

Salto [32], [33] is an example of a hopping robot equipped with SEA. Salto resolved the problem of premature release of elastic energy by tuning the mechanical advantage, i.e., the ratio of output force to input force. During the energy storage phase when the foot is in contact with the ground, the linkage leg of Salto has low mechanical advantage. With the low mechanical advantage, Salto could not produce an output force higher than its own weight although the input is higher than its own weight. As a result, Salto is able to bend its leg for a longer period to store more energy in the elastic element until the mechanical advantage switches to a higher value. However, the specific mechanical advantage profile required for storing higher elastic energy limits the motion range of the actuator and prevents the actuator from continuously rotating in one direction. Therefore, the combination of SEA and specific mechanical advantage profile could not generate a cyclic foot trajectory.

II. General Concept of Inverted Cam

Here, we propose a novel elastic actuation system, called the inverted cam (see Fig. 2), to combine a cyclic trajectory and power modulation with controlled energy charge and release. The inverted cam inverts the stationary and rotary parts from a conventional eccentric cam. It consists of a crank for the appendage linkage and a cam-shaped shell with a gradually decreasing radius. The crank is connected to the output shaft of the motor and rotates inside the cam-shaped shell. The crank consists of the following three parts: two links (light and dark orange in Fig. 2) connected to each other through a torsion spring. This connection makes the motor and the crank an SEA with the torsion spring acting as the elastic element. Although regular SEA stores energy passively, the inverted cam stores elastic energy in the torsion spring like a PEA by forming a parallel structure with the cam-shaped shell as the crank rotates inside the shell (Fig. 2 right diagram). Because of this quasi-parallel-elastic structure, the elastic energy is determined by the output shaft angular position when the crank is inside the cam-shaped shell. As the tip of the crank moves along the cam-shaped shell, the reducing shell radius exerts a force to compress the torsion spring in the crank. At the end of the cam-shaped shell, the crank loses contact with the shell, and the torsion spring releases the stored elastic energy.

This mechanism provides the advantage of having both series and PEA characteristics by coupling the SEA with the cam-shaped shell in parallel. The energy-charging strategy of this quasi-PEA increases the elastic energy capacity by enabling the actuator to control energy capacity by pressing the elastic element onto the cam shell. At the moment of energy release, the parallel connection breaks, and the elastic energy is released. By shifting the mode between quasi-parallel-elastic and series-elastic, the system combines the advantages of high elastic energy capacity offered by PEA and of cyclic trajectory offered by SEA.

The inverted cam also has the nice property that the electric motor continuously turns in the same direction (i.e., there is no back and forth movements). The continuous rotation of the motor allows a fast locomotion frequency because the motor does not have to change direction during the locomotion cycle. In addition, producing cyclic trajectory through the continuous motor rotation allows a system to have initial velocity in favor of the motion before the release of elastic energy.
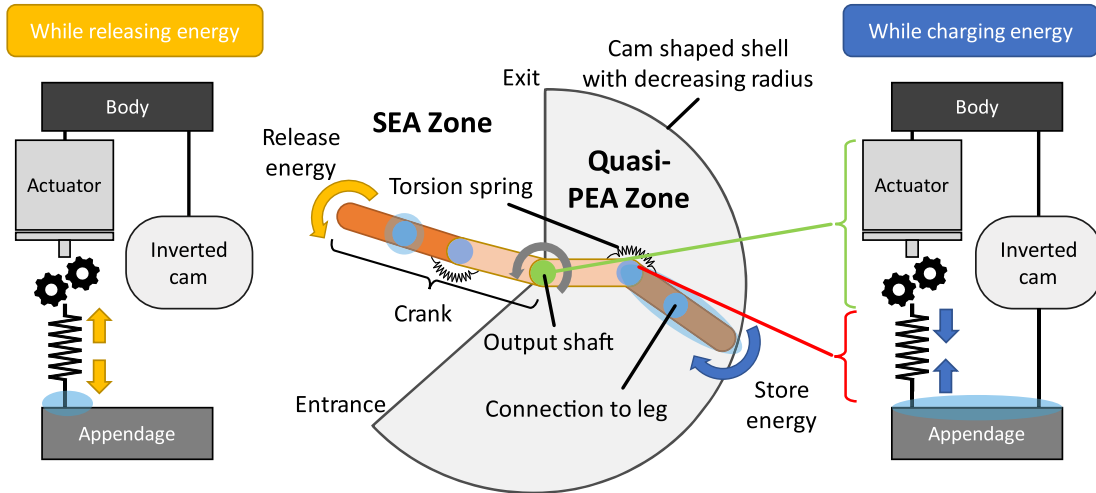
Fig. 2.   Inverted cam diagrams. The middle diagram shows the inverted cam with the modes specified with the texts "SEA Zone" and "quasi-PEA" Zone. The quasi-PEA zone is when the crank has contact with the radius reducing shell to bend the embedded torsion spring and store energy. The blue shaded regions indicate the connection between the leg and the crank. SEA zone is where the crank loses the contact with the radius reducing shell and releases the stored elastic energy. The left and right diagram pictorially show the status of the SEA zone and quasi-PEA zone, respectively. The yellow and blue arrows on the compression springs indicates the direction of the spring deformation.

In order to validate the proposed mechanism, we built a one-legged hopping platform that is equipped with the inverted cam and capable of continuous repeated hopping. We aimed to build a 150 g platform with 15 cm × 15 cm based on the choice of the electric motor.

The rest of this article is organized as follows. We characterize the inverted cam, describe the appendage design of the proposed system, provide the modeling and corresponding simulation of hopping performance, and finally validate the design with experimental results obtained with the one-legged prototype.

III. INVERTED CAM CHARACTERIZATION

A. Input Torque Calculation

The inverted cam allows for customization of the maximum amount of stored elastic energy based on the application as well as the required motor input torque. For a given maximum stored energy, it is important to be able to design the motor input torque profile. Doing this requires a model, thus, in this section, we develop and validate one.

The required input motor torque profile to fully charge the torsion spring can be determined using the principle of virtual work. Fig. 3 shows the inverted cam parameters used for the torque calculation. Assuming no friction losses, the work of the inverted cam output shaft must be used to store the energy in the torsion spring, thus

$$\delta W_o = \delta W_s \qquad (1)$$

where δW_o is the work from the inverted cam output shaft and δW_s is the work done on the spring. Because work is torque times the change of angle, (1) can be rewritten as

$$\tau_o \delta \theta_o = \tau_s \delta \theta_s \qquad (2)$$
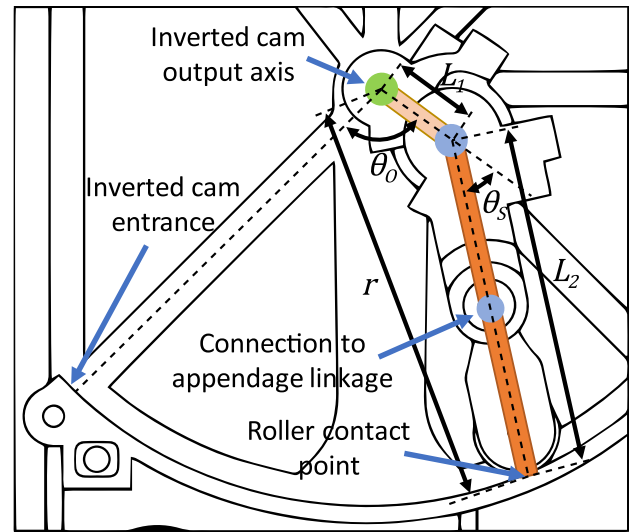
Fig. 3.   Parameters of the inverted cam. L_1 and L_2 are the lengths of the links consisting of the crank. r is the length of the third side of the triangle formed by L_1 and L_2 links. θ_O is the output shaft angle with respect to the inverted cam entrance. As θ_O increases, r decreases due to the increase in the spring angle, θ_S.

where τ and $\delta \theta$ with subscripts are torque and change in angle, respectively. The subscript o indicates output shaft and s indicates spring. Spring torque equals the spring constant k_s, times the spring angle θ_s, and the zero deflection angle of the spring $\theta_{s,i}$, therefore, (2) can be rewritten as

$$\tau_o = k_s(\theta_s + \theta_{s,i}) \frac{\delta \theta_s}{\delta \theta_o} \qquad (3)$$

where $\frac{\delta \theta_s}{\delta \theta_o}$ is determined by the lengths of L_1 and L_2 and the shell radius function, $r(\theta_o)$. Specifically, the relationship between θ_s

and θ_o is

$$\theta_s = \pi - \arccos \frac{L_1^2 + L_2^2 - r^2(\theta_o)}{2L_1 L_2}. \tag{4}$$

$r(\theta_o)$ is specific to the inverted cam design. For the prototype developed here, a linear function is used

$$r(\theta_o) = -\frac{L_1 + L_2 - r_f}{\theta_{o,f}} \theta_o + L_1 + L_2 \tag{5}$$

where r_f and $\theta_{o,f}$ are the radius of the cam-shaped shell and the inverted cam output shaft angle at the exit of the cam-shaped shell, respectively. r_f is defined using the law of the cosine for the triangle formed by link L_1 and link L_2

$$r_f = \sqrt{L_1^2 + L_2^2 - 2L_1 L_2 \cos(\pi - \theta_{s,\max})}. \tag{6}$$

Equations (4)–(6) can be plugged into (3) to calculate the output shaft torque required to operate the cam. Because there is a gearbox placed between the inverted cam output shaft and the motor output shaft, the relationship between the inverted cam output torque, τ_o, and the motor torque, τ_m, is

$$\tau_m = \frac{\tau_o}{c_{\text{GR}}} \tag{7}$$

where c_{GR} is the reduction ratio of the gearbox.

The maximum amount of elastic energy in the torsion spring $E_{s,\max}$ is determined by the choice of spring constant k_s and the maximum torsion spring angle $\theta_{s,\max}$ as shown in the following equation:

$$E_{s,\max} = \frac{1}{2} k_s \theta_{s,\max}^2. \tag{8}$$

B. Validation

To validate the theoretical model, we measured the motor torque values through experimentation. We installed two 1 Ω resistors in parallel in between the motor controller and the voltage regulator (see Fig. 4). We could not install the resistors between the motor and motor controller to directly measure the motor torque because a flex cable was connecting between the motor and the motor controller. We used an oscilloscope to measure the voltage drop over the installed resistors while the motor was operating the inverted cam system. The measured voltage could be converted to current with Ohm's law. We also measured the average current used to only operate the motor controller and subtracted this value from the current measurement in order to get the current used only for the motor. With known stall torque and stall current of the motor, the measured current could be converted to motor torque. The information about the motor, motor controller, and the gearbox is presented in Section VI-A. The parameters used for the simulation and experiment are shown in Table I.

With the test setup, we obtained motor torque values with motor speed from 1000 to 10 000 r/min with an interval of 1000 r/min. For each motor speed, we ran the motor while the inverted cam operated for five cycles and recorded three trials. Since the motor output shaft torque was transmitted to the inverted cam output shaft through a three step gearbox with a c_{GR} of 61.875,
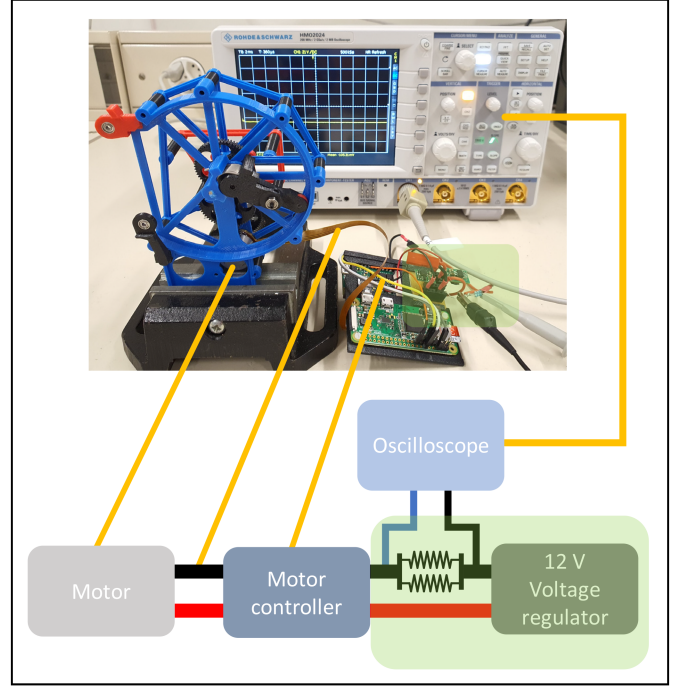

Fig. 4. Experimental setup of motor torque measurement. The red line connecting the components is the power, and the black line is the ground. In between the motor controller and the voltage regulator, two 1 Ω resistors were placed in parallel. The voltage drop over the resistors was measured and converted to current using Ohm's law with the known resistance value.

TABLE I
INVERTED CAM PARAMETERS

Parameter	Value
L_1	0.01 m
L_2	0.04 m
$\theta_{s,i}$	90°
$\theta_{s,\max}$	87°
$\theta_{o,f}$	270°
k_s	0.0709 N·m/rad
c_{GR}	61.875

the output shaft of the inverted cam rotated 61.875 times slower than the motor output shaft.

The theoretical motor output shaft torque values are presented in Fig. 5 alongside experimental results for motor speed of 7000 r/min. To reduce the effect of the transient behavior related to the motor dynamics, we neglected the first cycle and plotted only the second, third, and fourth cycles. Just one motor speed is selected for the plot because the comparison between experimental results and theoretical calculations at different motor speed were similar to each other. 7000 r/min is selected because this is the motor speed used for the hopping experiment. As was predicted by the theoretical calculation, the motor generated the highest torque at the beginning, and then exponentially decreased as the tip of the crank approached the exit of the inverted cam. It was observed that the measured torque values were higher than the theoretically calculated torque values except the very beginning of each cycle. This phenomenon is likely caused by friction from the rough surfaces of the inverted cam, gears, and joints and imperfect alignment of the gears. The uneven surfaces on the
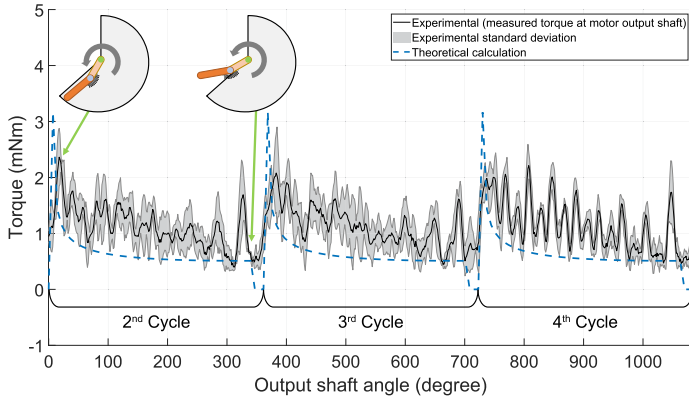
Fig. 5.   Theoretical calculation and experimental results of the motor torque profile during the continuous three cycles of cam operation. Three trials are shown with the solid black line (mean) and the shaded region (standard deviation). Both the theoretical calculation and experimental results had exponentially decreasing torque profiles. However, the measured motor torque was higher than the theoretical calculation throughout the entire profile. The motor operated at 7000 r/min, which resulted in 1.89 Hz at the inverted cam output shaft.

inverted cam, joints, and gears required extra torques at random moments. Thus, the noise was generated in an unpredictable way. By taking an integral of the motor torque profile over the motor angle in radian, the total mechanical energy input can be obtained. The average energy input for one cycle from the motor and the energy stored in the spring were 0.44 J and 0.25 J, respectively. Thus, the mechanical efficiency of the inverted cam was 57.2% at 7000 r/min. These losses stem from friction in joints and gear mesh and could probably be reduced with higher quality construction.

The electric efficiency was also calculated based on the consumed electric energy. The average electric energy used per one cycle at 7000 r/min was 1.21 J, and this number corresponds to 20.8% energy efficiency. This extra loss is due to the motor inefficiency including the joule heating loss.

IV. APPENDAGE DESIGN

For a hopping platform, the appendage needs to generate a foot trajectory with both a stance and swing phase. During the stance phase, the foot is in contact with the ground and has to push the body forward and off the ground by releasing the stored energy in the inverted cam. While the swing phase, the foot is in the air and the appendage needs to bring the foot back to the starting point of the stance phase for the next cycle.

A Stephenson type III linkage [43] produces a close approximation of the desired foot trajectory and is used as a starting point for a further design refinement process. The final design of the leg linkage was found through iterations of simulations based on a dynamic modeling and experiments with actual prototypes. The current leg linkage design (see Fig. 6) has a relatively flat foot trajectory to push the body forward at the beginning of the stance phase (Stance phase w/o spring activation in Fig. 6) and a curved-down foot trajectory at the end of the foot trajectory to take off (Stance phase w/ spring activation in Fig. 6). This foot trajectory also has a swing phase that does not overlap with the stance phase to prevent the system from an early touchdown [44].
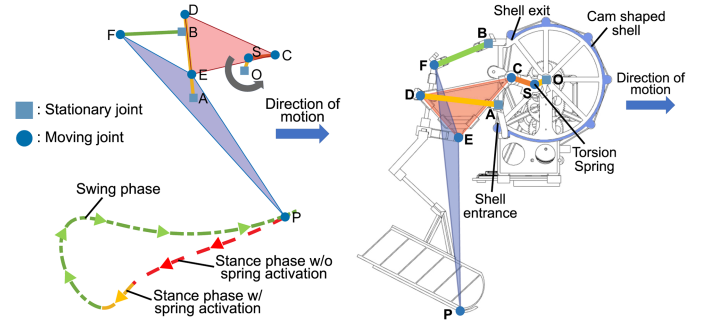

Fig. 6.   Linkage design with corresponding foot trajectory (left) and a CAD model of the linkage on the robot (right). The alphabets indicate the joints, and the colored rigid bodies and the solid lines indicate the links. The foot trajectory is drawn when the crank indicated with "O–S–C" rotates counter-clockwise around joint "O."

TABLE II
LEG LINKAGE PARAMETERS

Parameter	Value (cm)
A	[–3.81,–2.02]
B	[–4.67,2.91]
$\overline{BF}$	4.46
$\overline{AD}$	6.25
$\overline{CD}$	7.38
$\overline{CE}$	6.40
$\overline{DE}$	4.50
$\overline{EF}$	6.10
$\overline{EP}$	12.71
$\overline{FP}$	18.34

The leg linkage parameters are tabulated in Table II. The status of the prototype, inverted cam, and energy level throughout the entire cycle is shown in Fig. 7.

V. MODELING AND SIMULATION

A mathematical model using the Lagrange formulation was derived to simulate the hopping performance of the robotic platform equipped with the inverted cam and six-bar leg linkage. The robotic system was modeled as a floating base [45] in a two-dimensional space (see Fig. 8). We used five generalized coordinates ($\mathbf{q} \in \mathbb{R}^5$) to represent the system. The horizontal and vertical positions with respect to the base frame were represented as q_1 and q_2, respectively, and q_3 was used to represent the pitch rotation. To simplify the dynamics of the multiple links in the leg linkage, the crank of the inverted cam, and leg linkage were assumed to be a single appendage with an actuated revolute joint (q_4) and prismatic joint (q_5).

A. Input Calculation

To use the generalized coordinates q_4 and q_5, we need to know how to map the inverted cam output shaft angle, θ_O, in Fig. 9 to q_4 and q_5. We first obtain the inverted cam crank kinematics. Then, we calculated the corresponding foot trajectory kinematics. The schematic of the inverted cam crank is shown in Fig. 9, and the position and corresponding acceleration of joint C, $\mathbf{p}_C$ and $\ddot{\mathbf{p}}_C$,
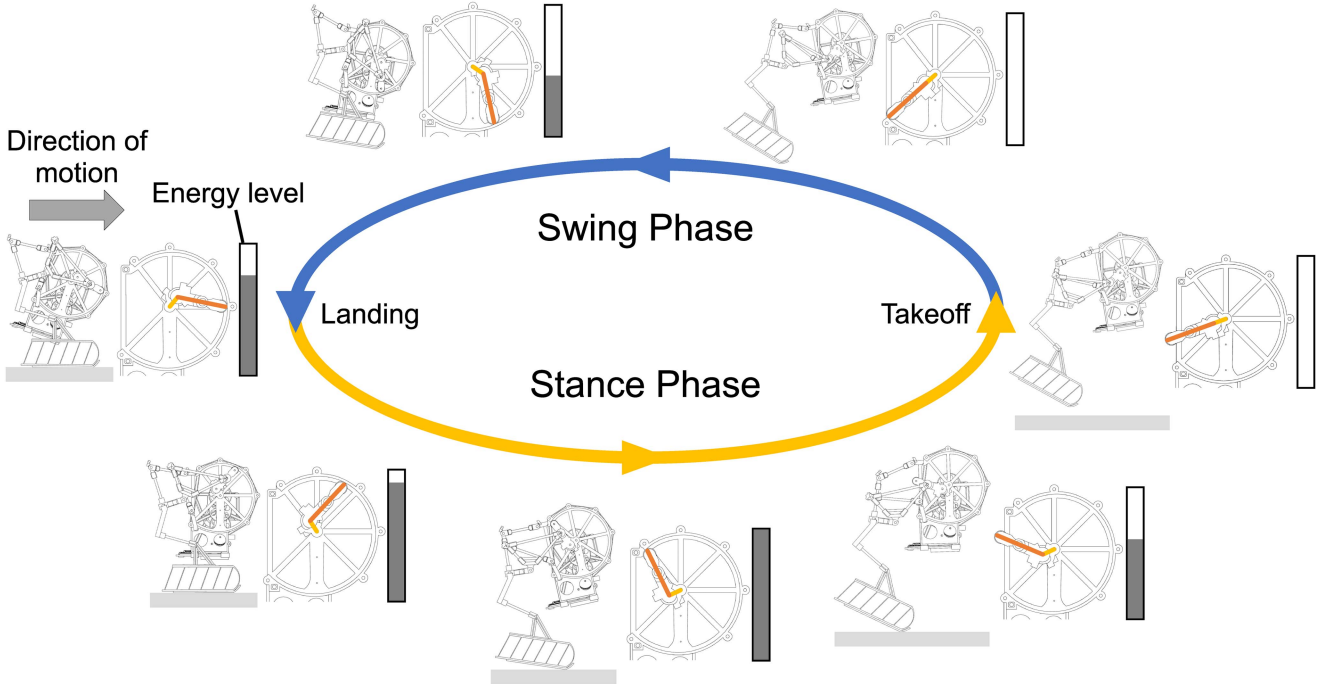
Fig. 7. Status of the hopper, inverted cam, and energy during a cycle. The grey bar indicates the energy level changes in the torsion spring as the robot follows the locomotion cycle. The yellow and orange bars are the crank of the inverted cam and presents the change in spring angle. The CAD rendering of the entire platform shows how the leg linkage changes as the crank rotates over the cycle.
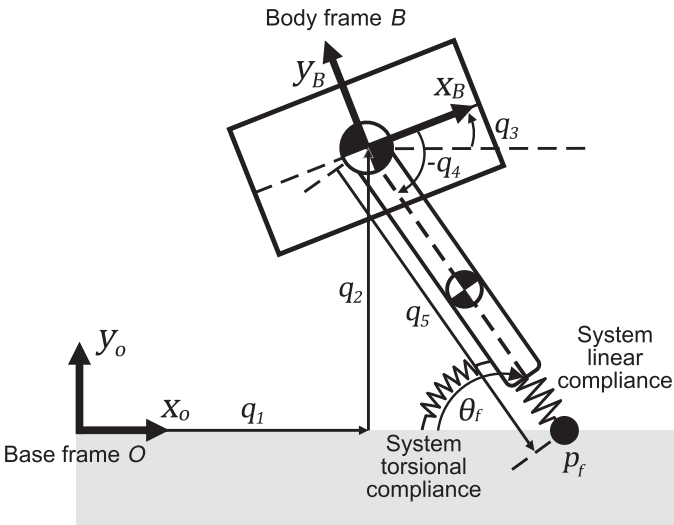

Fig. 8. Schematic for the robot model. Generalized coordinates (q_1–q_5) are used to model the robot. q_4, the leg angle, and q_5, the leg length, are defined with respect to the "B" frame and are the actuated coordinates. There is a constraint at the foot point "p_f." One linear spring and one torsional spring are connected to the leg.

Fig. 9. Schematic for inverted cam crank. The crank consists of two links and one torsion spring. Joint "O" is the output axis of the inverted cam, joint "S" is where the torsion spring is embedded, and joint "C" is where the power from the crank is transmitted to the leg. θ_O is the output shaft angle, and θ_S is the spring angle.

can be expressed as

$$\mathbf{p}_C{}^O = \mathbf{p}_S{}^O + \mathbf{R}_S^O \mathbf{p}_C{}^S, \quad \mathbf{p}_S{}^O = \overline{OS} \begin{bmatrix} \cos\theta_O \\ \sin\theta_O \end{bmatrix} \quad (9)$$

$$\ddot{\mathbf{p}}_C{}^O = \ddot{\mathbf{p}}_S{}^O + \ddot{\mathbf{R}}_S^O \mathbf{p}_C{}^S + 2\dot{\mathbf{R}}_S^O \dot{\mathbf{p}}_C{}^S + \mathbf{R}_S^O \ddot{\mathbf{p}}_C{}^S \quad (10)$$

where the superscripts and subscript in $\mathbf{p}$ describe the frame where the term is described in and the joint name, respectively. $R_{\text{From}}^{\text{To}} \in \mathrm{SO}(2)$ is a rotation matrix whose superscript represents the frame after transformation and subscript represents the current frame. In (9) and (10), the only variable is θ_O, and the other terms are determined by the geometry of the crank and θ_O. We assume that the motor is controlled at a constant angular velocity. Therefore, $\ddot{\mathbf{p}}_S{}^O$ only has a normal direction acceleration and can be written as

$$\ddot{\mathbf{p}}_S{}^O = -\frac{\|\dot{\mathbf{p}}_S{}^O\|^2}{\overline{OS}} \hat{\mathbf{x}}_S{}^O \quad (11)$$

where the hat indicates a unit vector. The position, velocity, and acceleration of point C with respect to frame S are

$$\mathbf{p}_C{}^S = \mathbf{R}_C^S \begin{bmatrix} \overline{SC} \\ 0 \end{bmatrix} \tag{12}$$

$$\dot{\mathbf{p}}_C{}^S = \overline{SC}\omega_s\hat{\mathbf{y}}_C{}^S \tag{13}$$

$$\ddot{\mathbf{p}}_C{}^S = -\frac{\|\dot{\mathbf{p}}_C{}^S\|^2}{\overline{SC}}\hat{\mathbf{x}}_C{}^S + \alpha_s\overline{SC}\hat{\mathbf{y}}_C{}^S \tag{14}$$

where ω_s and α_s are the angular velocity and acceleration of point C rotating around joint S. When the roller on the crank is making contact with the cam-shaped shell, ω_s and α_s can be calculated using geometry with a given motor angular speed. When the roller loses contact with the shell, the spring on joint S releases energy, and the corresponding angular acceleration is

$$\alpha_s = \frac{\tau_s}{I_{SC}} \tag{15}$$

where τ_s is the spring torque and I_{SC} is the inertia of link SC. τ_s can be calculated using

$$\tau_s = -k_s(\theta_s + \theta_p) \tag{16}$$

where k_s is the torsion spring constant and θ_p is the zero deflection angle of the spring. The prototype had a value of $-\frac{\pi}{2}$ for θ_p.

With (10)–(16), the positions of joint C can be determined for the entire cycle using a differential equation solver. The known kinematics of joint C are then used to calculate the corresponding foot kinematics with the known leg linkage geometry. Then, q_4 becomes the angle with respect to the body frame in Fig. 8, and q_5 becomes the length of the vector connecting the foot and the center of mass of the body. Taking derivatives of the known q_4 and q_5 values, the required $\ddot{q}_4$ and $\ddot{q}_5$ and corresponding input torque and force can be determined.

B. Modeling for Different Phases

To provide a nonslipping condition on the foot, we assumed that the foot is a pin joint by making a constraint at the foot with the ground [45], [46]. The constraint conditions are zero velocity and acceleration at the foot, which are

$$\dot{\mathbf{p}}_{\mathbf{f}} = \mathbf{J}_c\dot{\mathbf{q}} = 0 \tag{17}$$

$$\ddot{\mathbf{p}}_{\mathbf{f}} = \mathbf{J}_c\ddot{\mathbf{q}} + \dot{\mathbf{J}}_c\dot{\mathbf{q}} = 0 \tag{18}$$

where $\mathbf{p}_{\mathbf{f}}$ is the foot position, and $\mathbf{J}_c$ is a Jacobian matrix, are

$$\mathbf{p}_{\mathbf{f}} = \begin{bmatrix} q_1 \\ q_2 \end{bmatrix} + \mathbf{R}(q_3 + q_4)\begin{bmatrix} q_5 \\ 0 \end{bmatrix} \tag{19}$$

$$\mathbf{J}_c = \frac{\partial \mathbf{p}_{\mathbf{f}}}{\partial \mathbf{q}}. \tag{20}$$

The equation of motion of the model with the foot constraint is

$$\mathbf{M}\ddot{\mathbf{q}} + \mathbf{C}\dot{\mathbf{q}} + \mathbf{g} + \mathbf{J}_c^{\mathbf{T}}\mathbf{F}_c = \mathbf{S}^{\mathbf{T}}\boldsymbol{\tau} + \mathbf{F}_{\mathbf{ext}} \tag{21}$$

where $\mathbf{M}$ is the mass and inertia matrix, $\mathbf{C}$ is the centrifugal and Coriolis effect matrix, $\mathbf{g}$ is the gravitational force vector, $\mathbf{F}_{\mathbf{c}}$ is the reaction force vector at the foot, $\mathbf{S}^{\mathbf{T}}$ is the matrix

TABLE III
SIMULATION PARAMETERS

Parameter	Value
m_{body}	0.124 kg
m_{leg}	0.026 kg
I_{body}	1.86×10^{-4} kg·m²
I_{leg}	9.19×10^{-5} kg·m²
I_{SC}	1.0×10^{-4} kg·m²
I_b	2.37×10^{-2} kg·m²
L_b	1 m
k_l	1400 N/m
k_t	1.02 Nm/rad
θ_p	90°
$\theta_{f,i}$	62°

that maps two by one input vector to generalized coordinates for a dimension match [45], $\boldsymbol{\tau}$ is the actuator input vector, and $\mathbf{F}_{\mathbf{ext}}$ is the external force vector. $\mathbf{F}_{\mathbf{ext}}$ contains the force and torque on the leg created from the springs. In addition, it captures the effects of boom inertia acting against the rotation around the boom. The effects of a boom are required because although the simulation is in two-dimensional space, the actual platform was connected to a boom and hopped around in a circle (see Section VI experimental method). The linear spring force, torsional spring torque, and inertia effect are

$$\mathbf{F}_l = k_l(q_{5,o} - q_5) \tag{22}$$

$$\mathbf{F}_t = k_t(\theta_f - \theta_{f,i}) \tag{23}$$

$$\mathbf{F}_b = -\frac{I_b\boldsymbol{\alpha}_b}{L_b} \tag{24}$$

respectively, where k_l is the linear spring constant, k_t is the torsion spring constant, $q_{5,o}$ is q_5 without spring deformation, $\theta_{f,i}$ is the angle between the leg and the ground, $\theta_{f,i}$ is the angle between the leg and the ground at the beginning of stance phase, I_b is the boom inertia, L_b is the boom length, and $\alpha_{\mathbf{b}}$, is the angular acceleration of the system. Once the model reached the condition for take-off, we removed the nonslipping condition on the foot and the effects of the springs, and the equation of motion simply becomes

$$\mathbf{M}\ddot{\mathbf{q}} + \mathbf{C}\dot{\mathbf{q}} + \mathbf{g} = \mathbf{S}^{\mathbf{T}}\boldsymbol{\tau} + \mathbf{F}_{\mathbf{ext}}. \tag{25}$$

After take-off, we considered the effect of leg retraction to the initial configuration in the dynamics. The external force only contained the effect of the boom during the swing phase. The parameters used for the simulation are presented in Table III where m, I, and L refers to the mass, inertia, and length, respectively. These values were obtained from a computer-aided design (CAD) model. k_l and k_t were estimated from experiments.

C. Simulation Results

Fig. 10 shows the simulation results of three continuous hopping data for position, velocity, and pitch angle. In average, the robot was able to travel 18.2 cm and 12.4 cm in horizontal and vertical direction, respectively, for each hop. The velocity plot showed that the velocities in both x- and y-direction suddenly increased when the spring is activated. The velocity increase in y-direction was higher because the foot trajectory had steeper
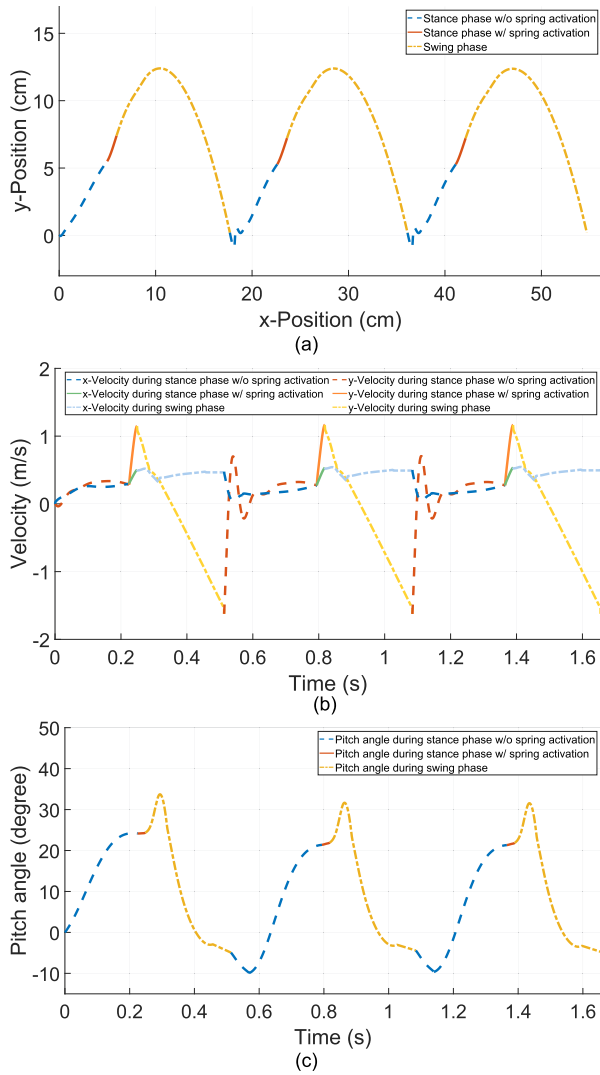
Fig. 10. Simulation results with the dynamic modeling. (a) Center of mass trajectory. (b) Velocity versus time plot. (c) Pitch angle versus time plot. The trajectory plot is divided into three sections. For each line, three different line styles and colors are used to indicate the three different phases of the hopping cycle.
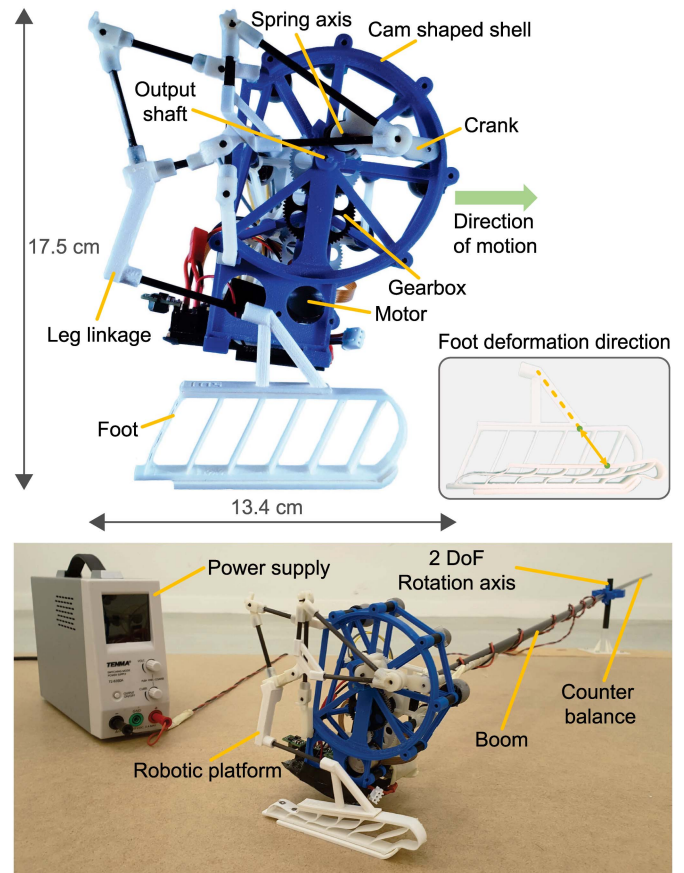

Fig. 11. Prototype and experimental setup pictures. The boom system is counter balanced by connecting the same sized bar on the other side. The robot can be operated by on-board battery or external power supply. For a long-term experiment, the robot was powered by a power supply, but the robot carried a battery to keep the weight.

change in y-direction, as shown in Fig. 6. The peak x-velocity was 0.54 m/s, and the peak y-velocity was 1.16 m/s in average. The pitch angle increased to $22.3°$ in average before the spring activation. No significant change in the pitch angle was observed during the spring activation. Once the robot entered swing phase, the pitch angle suddenly increased up to $32.3°$ and decreased again to $-4.7°$ due to the leg retraction. During this time, the motor controller on the physical prototype was entering an error mode when there was a sudden change in the speed, thus, the system required a certain amount of time to reset the motor. This delay was accounted for in the simulation. The three hops took 1.65 s, and the corresponding frequency was 1.82 Hz. From this simulation, we verified that the inverted cam is able to provide power modulation and produce repetitive hopping through cyclic trajectory. We will compare the simulation results to the real robot behavior in Section VII.

VI. EXPERIMENTAL METHOD

A. Prototype

A one-legged hopping robot was built to experimentally validate the simulation and inverted cam concept (see Fig. 11). The inverted cam shell, gears, and body parts were 3-D printed with ABS plastic. Gear shafts were cut from 2 mm and 3 mm diameter stainless steel rods. Carbon fiber rods were used for the leg linkages and to assemble 3-D printed parts consisting the inverted cam structure. Bearings were used to provide smooth rotation in the joints and gearbox. The electric motor was a Maxon EC 20 flat 351005 model. This motor provided nominal torque of 7.59 mN · m and no-load speed of 10 000 r/min. In the experiment, the motor speed was set to 7000 r/min during the stance phase and was set to 10 000 r/min during the swing phase to quickly retract the leg and prepare landing. It was connected to a gearbox consisting of 3-D printed gears with 1:61.875 gear reduction rate via three steps. An ESCON Module 24/2 from Maxon was used as the motor controller, as this controller provides speed control using an embedded hall effect sensor in the motor. A Raspberry pi zero W was used as the microcontroller. The robot could be powered by a 2 cell Li-Po battery with 180 mAh, but a power supply was used during the experiment to

TABLE IV
WEIGHT BREAKDOWN

Item	Value (g)
Inverted Cam (Including gearbox)	39.42
Leg Linkage	23.51
Motor (Maxon EC 20 flat 351005)	21.4
Motor controller (ESCON Module 24/2)	13.87
Micro controller (Raspberry Pi Zero W)	9.09
Li-Po Battery (2 Cell, 180 mAh)	13.03
Voltage regulators	7.49
Electric component holder	6.6
Components for boom connection	23.31
Reflective markers	11.54
Total	169.26

avoid having to recharge the battery often. The weight of the robot excluding components for a boom connection (bearings and 3-D printed bearing mounts) and reflective markers was 134 g, and the total was 169 g. A weight breakdown is presented in Table IV.

The foot was 3-D printed with TPU 95 A. The model shown in Fig. 8 captures the spring-like characteristics of the TPU 95 A through the combination of linear and torsional springs. The angled struts in Fig. 11 were providing directionality to align the deformation direction with the line connecting the center of mass and the very front of the foot, as shown in Fig. 8. The flexible foot could also deflect like a torsional spring. Two ABS plates were attached on the top and bottom surfaces of the foot to prevent uneven deformation of the foot. To be statically stable on the ground in a two-dimensional space, the center of mass projection on the ground must stay inside the contact line formed by the foot. The length of the foot was chosen to be long enough with a safety margin of 3 cm to place the center of mass projection on the ground between the both ends of the foot when the robot is at the beginning of stance phase.

B. Experimental Setup

The prototype was connected to a boom system to eliminate the effects from yaw and roll rotations and to focus on the pitch moment balance, which is the only rotation direction that we considered in the two-dimensional model (see Fig. 11). The prototype was able to freely rotate in pitch direction and follow a circular path around the center of the boom system with a fixed radius of 1 m. A 1 m carbon-fiber rod was added to the opposite side of the boom from the prototype to counter balance the mass of the boom. The hopping trajectory was measured in a room equipped with an Optitrack motion capture system with 26 cameras that tracked the position and angle of reflective markers on the prototype at a rate of 120 Hz. A high-speed camera was also used for recording the experiment at 240 fps. The electric energy consumption from the motor was also measured using the same method used in Section III-B.

VII. EXPERIMENTAL RESULTS

As an example of a hop, video frames from one trial are shown in Fig. 12. During the stance phase ($\Delta t = 0$ ms to $\Delta t = 225$ ms in Fig. 12), the inverted cam simultaneously stored elastic energy in the torsion spring and pushed off the ground. In between Δt $= 225$ ms and $\Delta t = 300$ ms, the stored energy was released, and the motor and torsion spring together produced amplified peak power. While in the air, the leg continued to move and eventually came back to the starting posture ($\Delta t = 450$ ms) just before landing. While in the air, the inverted cam continued to store energy in the spring to be released for the next hop. The robotic platform stably landed on the ground and did not fall forward or backward. With the fast and continuous motor rotation, the entire cycle took around 525 ms. After landing, the platform was able to hop again by repeating the identical procedure.

A. Continuous Hopping Locomotion

The boom-connected prototype was commanded to continuously hop from a fixed starting point with the crouched posture (Fig. 12 $\Delta t = 0$ ms). A total of five trials of experimental hops were executed, and data, consisting of trajectory and pitch angle, were collected. From these data, horizontal and vertical velocity values were calculated. Mean values and standard deviations were obtained and compared with simulation results in Fig. 13.

In average, the robot horizontally traveled 56.0 cm for three hops, and the average horizontal and vertical distances traveled per one hop were 18.7 cm and 11.0 cm, respectively. We observed that the first hop was under performing compared to the following two hops. From the video recorded using the high-speed camera, we observed that the foot was slipping for the first hop, but the foot did not show significant slipping during the second and third hops. The average horizontal and vertical distances traveled per hop excluding the first hop were 20.4 cm and 11.5 cm, respectively. These numbers are 12.0% and 6.9% lower than the simulation results (18.2 cm and 12.4 cm).

In Fig. 13(b), the three different phases are indicated with different shaded regions. The hopping frequency was 1.82 Hz for the three hops and 1.70 Hz for the last two hops. The difference was coming from the lower height gain of the first hop (leading to a shorter step duration for the first hop). Both the x velocity and y velocity matched well with the simulation. At the beginning of the stance phase, velocities in both direction slowly increased until the spring activation phase. The sudden changes in both x and y velocities are observed during the stance phase with spring activation. Excluding the first hop, the average peak x and y velocities due to the spring activation were 0.54 m/s and 1.05 m/s, respectively. The percentage errors were 8.3% and 9.8%, respectively.

As the pitch plot shows in Fig. 13(c), the experimental data matched well with the simulation. In average, the pitch angle increased to 21.0° then decreased to 16.8° before the spring activation. The pitch angle suddenly increased to 34.1° after the spring activation and decreased to −4.7° until the end of the swing phase. These sudden changes in the pitch angle are observed in Fig. 12 with the orange arrows indicating the pitch angle. When the spring was activated ($\Delta t = 300$ ms), the fast backward swing of the leg caused the sudden change in the pitch angle. When the leg was quickly retracted forward ($\Delta t = 375$ ms), the pitch angle decreased again. The pitch angle kept

TABLE V
PROPERTIES OF JUMPING ROBOTS UNDER 1 KG WITH AN ELASTIC ACTUATION

Robot	Published year	Mass (g)	Size (cm)	Hopping height (cm)	Hopping distance (cm)	Energy charging time (s)	Hopping frequency (Hz)	Average forward velocity (m/s)	Froude number (-)	Energy per hop (J)	CoT (-)	Foot trajectory type	Actuation type
Glumper[a] [25]	2007	700	50	160	200	435	0.0023	0.0046	2.15×10^{-5}	80.5	**5.86**	Oscillatory	PEA
EPFL Jumper V1[b] [14]	2008	7	5	138	79	3.5	-	<0.23	<0.21	**1.23**	22.68	Oscillatory	PEA
EPFL Jumper V3[c] [15]	2010	14.33	18	62	46	3	0.13	0.061	2.13×10^{-5}	-	-	Oscillatory	PEA
Compact Kick-and-Bounce Robot [16]	2009	67	13	-	30	0.3	1.8	0.1	0.085	-	-	Oscillatory	PEA
Compact Jumping Robot[d] [29]	2010	18	11	16	33.33	-	3	1.06	5.59	-	-	Oscillatory	PEA
Grillo 3[a] [31]	2012	22	5	10	20	8	0.125	0.025	0.0025	-	-	Oscillatory	PEA
Flea Robot[a,b] [24]	2012	1.1	2.3	64	70	21	-	<0.033	0.0098	42.18	5584.02	Oscillatory	PEA
MSU Jumper[a] [27]	2013	23.5	6.5	87.2	89.8	10	0.067	0.060	0.011	-	-	Oscillatory	PEA
Jumpglider[c] [23]	2014	67.5	112	100	810	31.5	0.030	0.24	0.13	-	-	Oscillatory	PEA
TAUB[b] [17]	2015	23	13	335	137	20	-	<0.063	<0.032	11.91	38.54	Oscillatory	PEA
Jumping Module[a] [20]	2016	59.4	10	162	60	28	-	<0.021	$<9.36\times10^{-4}$	24.86	71.12	Oscillatory	PEA
SALTO 1-P [33]	2017	98.1	15	125.2	-	<0.22	1.52	**3.6 (max.)**	**17.61**	15	15.59	Oscillatory	SEA + Mechanical Advantage
This work	2022	169.2	17.5	11.5	20.4	0.4	1.7	0.35	0.14	2.09	6.43	Cyclic	SEA + Quasi-PEA

[a] The hopping frequency and average forward velocity are calculated only based on the energy charging time and self-righting time. Including the time in the air will decrease these values.
[b] The energy is calculated assuming that the voltage was constant during the experiments.
[c] Energy charging time or hopping frequency is estimated from the corresponding publication manuscript and video.
[d] Compact jumping robot uses two servo motors to twist a metal strip. Passive untwisting of the metal strip drives the jumping locomotion.
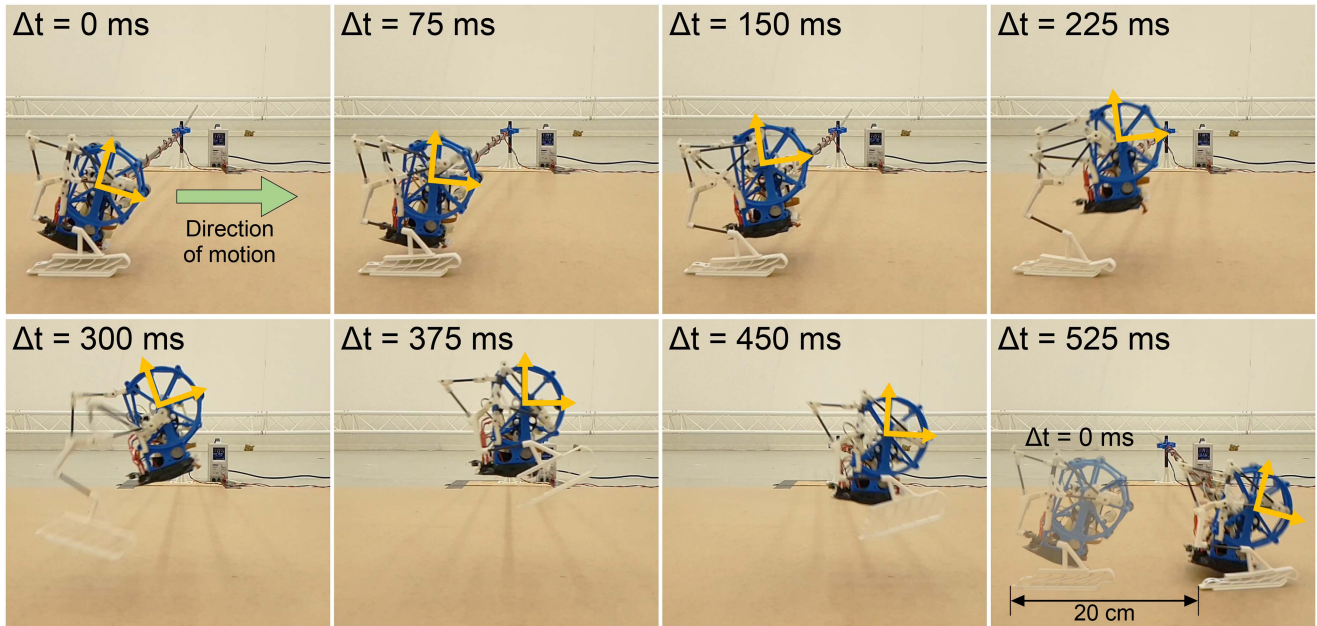

Fig. 12. Hopping in time sequence. The second hop among the three continuous hops is presented here. The hopping performance was recorded with a high-speed camera with 240 fps. Each frame has an interval of 75 ms. The orange arrows are presented to show the change in pitch angle. Note that there is an offset between the orange arrows and the measured pitch angle.

decreasing until the landing ($\Delta t = 525$ ms) and recovered to the original pitch angle.

Although the experimental and simulation results match well, there are sources of errors that created the slight differences between the simulation and experiments. First, the time required by the electric motor to accelerate to the desired angular velocity caused differences. Second, the simplification of six-bar linkage leg to a single link contributed to the differences. The inertia of the six-bar linkage leg changes at each moment, but, in the simulation, the leg inertia was fixed to the average value of the fully retracted and extended postures for simplicity. The center of mass position of the leg linkage also varies for different leg postures, but the center of mass position was assumed to be located at the middle of the leg model. To have a more accurate model, the dynamics of the six-bar linkage has to be considered [47]–[49]. Third, the foot slipping caused energy loss during the first hop. Fourth, the constant spring stiffness assumption for the torsional spring
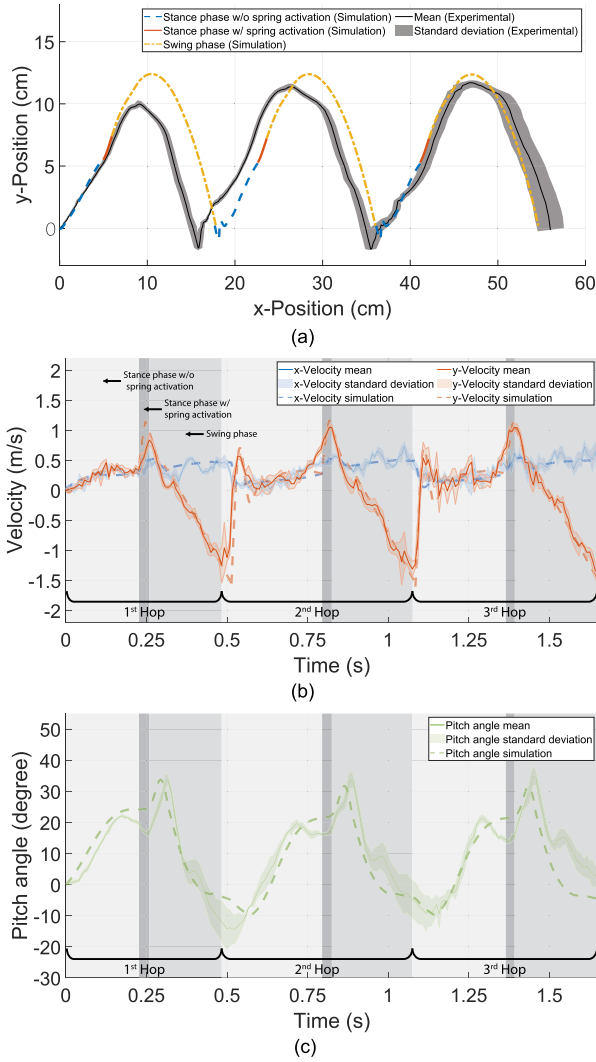
Fig. 13. Hopping experimental results. (a) Center of mass trajectory. (b) Velocity versus time plot. (c) Pitch angle versus time plot. Five sets of experimental data are collected. The mean values are shown in solid lines, and the standard deviation is shown with shaded regions. Simulation results are drawn with dashed lines.

characteristics of the TPU foot could contribute to the difference in the pitch angle. It is reported that compliant material springs have a reducing stiffness over their deflection [50]. In addition to these factors, friction in the six-bar leg linkage and vibration of the boom could also affect the experimental results.

B. Energetic Performance

We characterized the energetic performance of the system and plotted in Fig. 14. In Fig. 14(a), we observe that the kinetic, potential, and spring energy increases due to the energy input from the motor. During the stance phase with spring activation, energy transfer from the spring energy to kinetic and potential energies is observed with significant changes in the kinetic, potential, and spring energies. Right after the spring activation, the kinetic energy does not increase anymore but is transferred to potential energy. The total energy input from the motor for
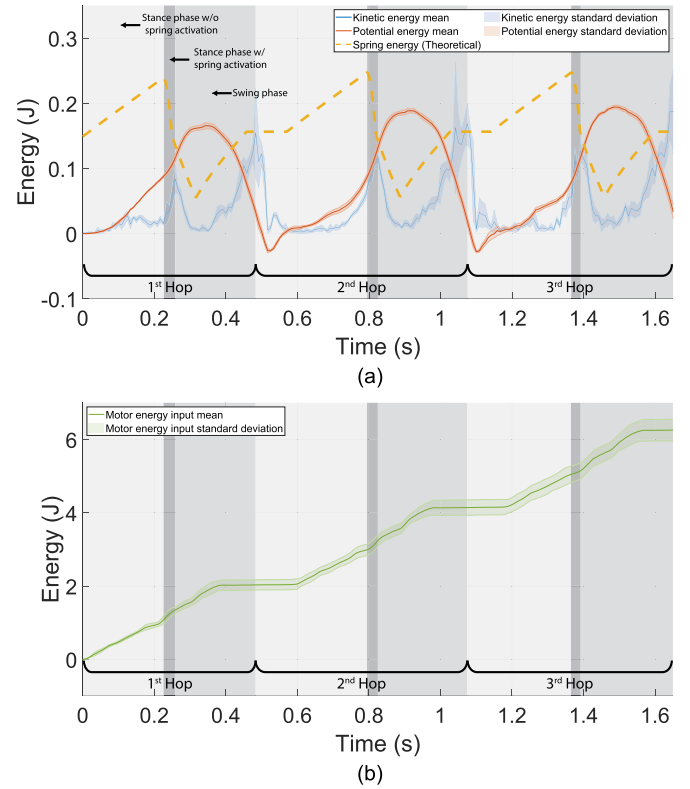

Fig. 14. Energy status versus time during the hopping. (a) Kinetic, potential, and elastic energy. (b) Energy input from motor. The kinetic energy and potential energy are calculated from the experimental velocity and height data. The spring energy is theoretically calculated with given spring constant and the change in the spring angle over time.

three hopping cycles is 6.26 J, and the average energy input per hop is 2.09 J.

A disadvantageous feature of the current platform is energy dissipation during the landing as the beginning of the second and third hop as shown in Fig. 14(a). Although biological and artificial systems for repeated hopping take advantage of elastic elements to recover part of the kinetic energy, our platform could not recover the kinetic energy because the foot has a low stiffness and shows spring bottoming out behavior for fixed frequency hopping. Recovering the kinetic energy using a stiffer foot requires detection of landing and precise timing control of the motor for a synergy with the foot, but the current platform does not have any sensors to implement such strategy. Adding extra sensors would enable the robot to improve energy efficiency with the help of foot energy recovery.

C. Comparison With Other Platforms

This article is compared with other robots under 1 kg equipped with elastic actuation in Table V. We only listed robots with enough information to compute the metrics on Table V, and the best performances of the last four metrics are in bold. To compare the speed, we used Froude number [51], [52], which is a dimensionless unit for size-independent speed comparison

and defined as

$$FR = \frac{v^2}{gl} \tag{26}$$

where v is a forward velocity, g is the gravitational acceleration, and l is a length characteristic of the motion. For this comparison, we selected l as the half of the platform height. With an average forward velocity of 0.35 m/s, our platform had a Froude number of 0.14. Among the robots capable of repeated hopping, our platform placed third. The robot with the best Froude number is SALTO 1-P [33], but the Froude number of SALTO 1-P was calculated based on the best single hop. SALTO 1-P has to hop vertically up after the long leap in order to balance itself. The compact jumping robot [29] has the second best Froude number of 5.59.

We also compared the energetic cost of transport (CoT) [52]–[54], which is defined as

$$CoT = \frac{E_{el}}{mgd} \tag{27}$$

where E_{el} electric energy consumed by the actuator, m is the robot mass, g is the gravitational acceleration, and d is the distance traveled by the platform. Our platform has a CoT of 6.43, which is the second best among the compared robots. The robot with the best CoT was Glumper [25] with a CoT of 5.86.

In addition, our platform with the inverted cam demonstrated balanced high-frequency continuous hopping. Balanced hopping and landing with a single-actuator leg required a self-righting strategy [15], [27], sprawling posture [16], [29], or extra actuators for balancing [33]. That last strategy also has advantages in more precise position control. The combination of cyclic appendage trajectory and power modulation with fixed amount of elastic energy and energy releasing moment allowed continuous erect posture hopping with a single actuator and feedforward actuator speed control.

VIII. Conclusion

This article introduces a new elastic actuation system called the inverted cam, which is designed to provide mobility through the combination of cyclic trajectory and controlled power modulation. The inverted cam is an SEA that becomes a quasi-PEA while storing energy by making a contact with a radius reducing shell. The decreasing radius of the shell bends the torsion spring embedded in the crank. The parallel energy charging strategy provides controlled energy charging time and releasing timing.

The relationship between the shell radius profile and required actuator torque to pass through the shell was studied using the virtual work principle to provide a design guide in the selection of radius profile and actuator. A linearly decreasing radius was tested in both simulations and experiments to validate the mathematical model. The mechanical and electric energy efficiencies of the inverted cam was 57.2 and 20.8%, respectively, at 7000 r/min motor speed. A dynamic modeling using Lagrangian formulation was derived to design the leg linkage that can generate hopping motion with the inverted cam. A 6-bar linkage was selected and tuned using the model and physical prototype iterations.

The robotic platform equipped with the inverted cam was constructed and tested on a boom. The robot was able to continuously hop forward at 1.82 Hz. The average horizontal and vertical distances traveled per hop was 18.7 cm and 11.0 cm in horizontal and vertical direction, respectively. The Froude number and energetic CoT for current prototype were 0.14 and 6.43, respectively.

These results show that the inverted cam is capable of combining cyclic trajectory with power modulation by controlled energy charge and release. The application of this technology is not limited to hopping. Other locomotion strategies that are based on cyclic trajectory and power modulation, such as flapping in the air or waving a tail fin under water could benefit from the inverted cam mechanism described here.

The inverted cam mechanism design has potential to be scaled. Because the ratio of L_1 and L_2 in Fig. 3 determines the mechanical advantage, reducing the length of L_1 allows a lower required motor torque, smaller cam-shaped shell size, and reduced weight. However, the current inverted cam design has a physical limitation that comes from the required space between the output shaft and the torsion spring rotation axis, thus the length of L_1 has a minimum limit. This limitation could be removed if a planetary gearbox is used instead.

In the future, we plan to explore the mechanism for bipedal locomotion. A bipedal system composed of a pair of inverted cams, appendages, and independent electric motors could be used to study the generation of diverse gaits, such as walking, running, and hopping.

References

[1] H. T. Henry, D. J. Ellerby, and R. L. Marsh, "Performance of guinea fowl Numida meleagris during jumping requires storage and release of elastic energy," *J. Exp. Biol.*, vol. 208, no. 17, pp. 3293–3302, Sep. 2005.

[2] G. N. Askew and R. L. Marsh, "Muscle designed for maximum short-term power output: Quail flight muscle," *J. Exp. Biol.*, vol. 205, no. 15, pp. 2153–2160, Aug. 2002.

[3] A. A. Biewener, "Muscle function in avian flight: Achieving power and control," *Philos. Trans. Roy. Soc. B. Biol. Sci.*, vol. 366, no. 1570, pp. 1496–1506, May 2011.

[4] M. J. Lighthill, "Hydromechanics of aquatic animal propulsion," *Annu. Rev. Fluid Mech.*, vol. 1, no. 1, pp. 413–446, Jan. 1969.

[5] R. E. Shadwick, H. S. Rapoport, and J. M. Fenger, "Structure and function of tuna tail tendons," *Comp. Biochem. Physiol. Mol. Integrative Physiol.*, vol. 133, no. 4, pp. 1109–1125, Dec. 2002.

[6] T. J. Roberts, "Muscular force in running turkeys: The economy of minimizing work," *Science*, vol. 275, no. 5303, pp. 1113–1115, Feb. 1997.

[7] T. Liu, K. Kuykendoll, R. Rhew, and S. Jones, "Avian wing geometry and kinematics," *AIAA J.*, vol. 44, no. 5, pp. 954–963, May 2006.

[8] R. M. Alexander and A. Vernon, "The mechanics of hopping by kangaroos (Macropodidae)," *J. Zoology*, vol. 177, no. 2, pp. 265–303, Aug. 1975.

[9] A. Galantis and R. C. Woledge, "The theoretical limits to the power output of a muscle–tendon complex with inertial and gravitational loads," *Proc. Roy. Soc. B.*, vol. 270, no. 1523, pp. 1493–1498, Jul. 2003.

[10] M. Ishikawa, P. V. Komi, M. J. Grey, V. Lepola, and G.-P. Bruggemann, "Muscle-tendon interaction and elastic energy usage in human walking," *J. Appl. Physiol.*, vol. 99, no. 2, pp. 603–608, Aug. 2005.

[11] T. J. Roberts and E. Azizi, "Flexible mechanisms: The diverse roles of biological springs in vertebrate movement," *J. Exp. Biol.*, vol. 214, no. 3, pp. 353–361, Feb. 2011.

[12] H. Bennet-Clark, "The energetics of the jump of the locust Schistocerca gregaria," *J. Exp. Biol.*, vol. 63, no. 1, pp. 53–83, Aug. 1975.

[13] R. M. Alexander, "Tendon elasticity and muscle function," *Comp. Biochem. Physiol., Mol. Integrative Physiol.*, vol. 133, no. 4, pp. 1001–1011, Dec. 2002.

[14] M. Kovac, M. Fuchs, A. Guignard, J.-C. Zufferey, and D. Floreano, "A miniature 7 g jumping robot," in *Proc. IEEE Int. Conf. Robot. Autom.*, 2008, pp. 373–378.

[15] M. Kovač, M. Schlegel, J.-C. Zufferey, and D. Floreano, "Steerable miniature jumping robot," *Auton. Robots*, vol. 28, no. 3, pp. 295–306, 2010.

[16] T. Tsuda, H. Mochiyama, and H. Fujimoto, "A compact kick-and-bounce mobile robot powered by unidirectional impulse force generators," in *Proc. IEEE/RSJ Int. Conf. Intell. Robots Syst.*, 2009, pp. 3416–3421.

[17] V. Zaitsev, O. Gvirsman, U. Ben Hanan, A. Weiss, A. Ayali, and G. Kosa, "A locust-inspired miniature jumping robot," *Bioinspiration Biomimetics*, vol. 10, no. 6, Nov. 2015, Art. no. 066012.

[18] B. G. Lambrecht, A. D. Horchler, and R. D. Quinn, "A small, insect-inspired robot that runs and jumps," in *Proc. IEEE Int. Conf. Robot. Autom.*, 2005, pp. 1240–1245.

[19] G.-P. Jung et al., "JumpRoACH: A trajectory-adjustable integrated jumping–crawling robot," *IEEE/ASME Trans. Mechatronics*, vol. 24, no. 3, pp. 947–958, Jun. 2019.

[20] G.-P. Jung, C. S. Casarez, S.-P. Jung, R. S. Fearing, and K.-J. Cho, "An integrated jumping-crawling robot using height-adjustable jumping module," in *Proc. IEEE Int. Conf. Robot. Autom.*, 2016, pp. 4680–4685.

[21] S. Stoeter, P. Rybski, M. Gini, and N. Papanikolopoulos, "Autonomous stair-hopping with Scout robots," in *Proc. IEEE/RSJ Int. Conf. Intell. Robots Syst.*, 2002, pp. 721–726.

[22] Q.-V. Nguyen and H. C. Park, "Design and demonstration of a locust-like jumping mechanism for small-scale robots," *J. Bionic Eng.*, vol. 9, no. 3, pp. 271–281, Sep. 2012.

[23] A. L. Desbiens, M. T. Pope, D. L. Christensen, E. W. Hawkes, and M. R. Cutkosky, "Design principles for efficient, repeated jumpgliding," *Bioinspiration Biomimetics*, vol. 9, no. 2, May 2014, Art. no. 025009.

[24] M. Noh, S.-W. Kim, S. An, J.-S. Koh, and K.-J. Cho, "Flea-inspired catapult mechanism for miniature jumping robots," *IEEE Trans. Robot.*, vol. 28, no. 5, pp. 1007–1018, Oct. 2012.

[25] R. Armour, K. Paskins, A. Bowyer, J. Vincent, and W. Megill, "Jumping robots: A biomimetic solution to locomotion across rough terrain," *Bioinspiration Biomimetics*, vol. 2, no. 3, pp. S65–S82, Sep. 2007.

[26] J. Burdick and P. Fiorini, "Minimalist jumping robots for celestial exploration," *Int. J. Robot. Res.*, vol. 22, no. 7/8, pp. 653–674, Jul. 2003.

[27] J. Zhao et al., "MSU jumper: A single-motor-actuated miniature steerable jumping robot," *IEEE Trans. Robot.*, vol. 29, no. 3, pp. 602–614, Jun. 2013.

[28] M. A. Woodward and M. Sitti, "MultiMo-Bat: A biologically inspired integrated jumping–gliding robot," *Int. J. Robot. Res.*, vol. 33, no. 12, pp. 1511–1529, Oct. 2014.

[29] A. Yamada, H. Mameda, H. Mochiyama, and H. Fujimoto, "A compact jumping robot utilizing snap-through buckling with bend and twist," in *Proc. IEEE/RSJ Int. Conf. Intell. Robots Syst.*, 2010, pp. 389–394.

[30] U. Scarfogliero, C. Stefanini, and P. Dario, "Design and development of the long-jumping "Grillo" mini robot," in *Proc. IEEE Int. Conf. Robot. Automat.*, 2007, pp. 467–472.

[31] F. Li et al., "Jumping like an insect: Design and dynamic optimization of a jumping mini robot based on bio-mimetic inspiration," *Mechatronics*, vol. 22, no. 2, pp. 167–176, Mar. 2012.

[32] D. W. Haldane, M. M. Plecnik, J. K. Yim, and R. S. Fearing, "Robotic vertical jumping agility via series-elastic power modulation," *Sci. Robot.*, vol. 1, no. 1, Dec. 2016, Art. no. eaag2048.

[33] D. W. Haldane, J. K. Yim, and R. S. Fearing, "Repetitive extreme-acceleration (14-g) spatial jumping with Salto-1P," in *Proc. IEEE/RSJ Int. Conf. Intell. Robots Syst.*, 2017, pp. 3345–3351.

[34] D. J. Blackman et al., "Leg design for running and jumping dynamics," in *Proc. IEEE Int. Conf. Robot. Biomimetics*, 2017, pp. 2617–2623.

[35] A. M. Johnson and D. E. Koditschek, "Toward a vocabulary of legged leaping," in *Proc. IEEE Int. Conf. Robot. Autom.*, 2013, pp. 2568–2575.

[36] A. De and D. E. Koditschek, "Parallel composition of templates for tail-energized planar hopping," in *Proc. IEEE Int. Conf. Robot. Automat.*, 2015, pp. 4562–4569.

[37] B. Katz, J. Di Carlo, and S. Kim, "Mini cheetah: A platform for pushing the limits of dynamic quadruped control," in *Proc. IEEE Int. Conf. Robot. Autom.*, 2019, pp. 6295–6301.

[38] A. Sayyad, B. Seth, and P. Seshu, "Single-legged hopping robotics research—A review," *Robotica*, vol. 25, no. 5, pp. 587–613, Sep. 2007.

[39] G. Pratt and M. Williamson, "Series elastic actuators," in *Proc. IEEE/RSJ Int. Conf. Intell. Robots Syst.*, 1995, pp. 399–406.

[40] Y. Yesilevskiy, W. Xi, and C. D. Remy, "A comparison of series and parallel elasticity in a monoped hopper," in *Proc. IEEE Int. Conf. Robot. Automat.*, 2015, pp. 1036–1041.

[41] T. Verstraten, P. Beckerle, R. Furnémont, G. Mathijssen, B. Vanderborght, and D. Lefeber, "Series and parallel elastic actuation: Impact of natural dynamics on power and energy consumption," *Mechanism Mach. Theory*, vol. 102, pp. 232–246, Aug. 2016.

[42] D. Paluska and H. Herr, "Series elasticity and actuator power output," in *Proc. IEEE Int. Conf. Robot. Autom.*, 2006, pp. 1830–1833.

[43] M. M. Plecnik and J. M. McCarthy, "Design of Stephenson linkages that guide a point along a specified trajectory," *Mechanism Mach. Theory*, vol. 96, pp. 38–51, Feb. 2016.

[44] A. R. Wu and A. D. Kuo, "Determinants of preferred ground clearance during swing phase of human walking," *J. Exp. Biol.*, vol. 219, no. 19, pp. 3106–3113, Oct. 2016.

[45] M. Hutter, "StarlETH & Co.: Design and control of legged robots with compliant actuation," Ph.D. dissertation, ETH Zürich, Zürich, Switzerland, 2013.

[46] Y. K. Ho, D. Wang, and Y. C. Soh, "Modelling of constrained robot system with constraint uncertainties," *J. Robot. Syst.*, vol. 17, no. 1, pp. 53–61, Jan. 2000.

[47] M. Plecnik, K. Fearing, and R. S. Fearing, "Adjustable power modulation for a leg mechanism suitable for running," in *Proc. IEEE Int. Conf. Robot. Automat.*, 2019, pp. 9137–9142.

[48] M. M. Plecnik and R. S. Fearing, "Designing dynamic machines with large-scale root finding," *IEEE Trans. Robot.*, vol. 36, no. 4, pp. 1135–1152, Aug. 2020.

[49] C. Liu and M. Plecnik, "The usage of kinematic singularities to produce periodic high-powered locomotion," in *Proc. IEEE/RSJ Int. Conf. Intell. Robots Syst.*, 2021, pp. 909–915.

[50] M. M. Plecnik, D. W. Haldane, J. K. Yim, and R. S. Fearing, "Design exploration and kinematic tuning of a power modulating jumping monopod," *J. Mechanisms Robot.*, vol. 9, no. 1, Feb. 2017, Art. no. 011009.

[51] R. Alexander, "Optimization and gaits in the locomotion of vertebrates," *Physiol. Rev.*, vol. 69, no. 4, pp. 1199–1227, Oct. 1989.

[52] A. Spröwitz, A. Tuleu, M. Vespignani, M. Ajallooeian, E. Badri, and A. J. Ijspeert, "Towards dynamic trot gait locomotion: Design, control, and experiments with cheetah-cub, a compliant quadruped robot," *Int. J. Robot. Res.*, vol. 32, no. 8, pp. 932–950, Jun. 2013.

[53] A. D. Kuo, "Choosing your steps carefully," *IEEE Robot. Autom. Mag.*, vol. 14, no. 2, pp. 18–29, Jun. 2007.

[54] S. Kim and P. M. Wensing, "Design of dynamic legged robots," *Found. Trends Robot.*, vol. 5, no. 2, pp. 117–190, Mar. 2017.

Won Dong Shin received the B.S. and M.S. degrees in mechanical engineering from the University of Illinois at Urbana-Champaign, Champaign, IL, USA, in 2016 and 2018, respectively. Since 2019, he has been working toward the Ph.D. degree in robotics with the Laboratory of Intelligent Systems, Ecole Polytechnique Federale de Lausanne, Lausanne, Switzerland.

William Stewart (Member, IEEE) received the M.S. and Ph.D. degrees in aerospace engineering from North Carolina (NC) State University, Raleigh, NC, USA, in 2014, and 2018, respectively.

From 2010 to 2014, he was a leader of the NC State University Aerial Robotics Team. From 2014 to 2016, he was a Research Assistant on the Eagle Ray project for the Smart Composites Laboratory. Since 2018, he has been a Postdoctoral Researcher with Laboratory of Intelligent Systems, Ecole Polytechnique Federale de Lausanne, Lausanne, Switzerland. His research interests include aerodynamics, mechanics, and vehicle design.

Dr. William is a two-time AUVSI student UAS competition champion (in 2010 and 2014).

Matt A. Estrada (Member, IEEE) received the B.S. degree in mechanical engineering from the Massachusetts Institute of Technology, Cambridge, MA, USA, in 2012 and the M.S. and Ph.D. degrees in mechanical engineering from Stanford University, Stanford, CA, USA, in 2015 and 2018, respectively.

From 2019 to 2021, he was a Postdoctoral Researcher with Biorobotics Laboratory, Ecole Polytechnique Federale de Lausanne, Lausanne, Switzerland.

Auke J. Ijspeert (Fellow, IEEE) received the engineering degree in physics from the Ecole Polytechnique Fédérale de Lausanne (EPFL), Lausanne, Switzerland, in 1995 and the Ph.D. degree in artificial intelligence from the University of Edinburgh, Edinburgh, U.K., in 1999.

Since 2002, he has been a Professor with EPFL, where he is currently the Head of Biorobotics Laboratory. His research interests include intersection between robotics, computational neuroscience, nonlinear dynamical systems, and applied machine learning. He is interested in using numerical simulations and robots to gain a better understanding of animal locomotion, and in using inspiration from biology to design novel types of robots and controllers. He is also investigating how to assist people with limited mobility using exoskeletons and assistive furniture.

Dr. Ijspeert is a member of the Board of Reviewing Editors of Science magazine, and an Associate Editor for the IEEE TRANSACTIONS ON MEDICAL ROBOTICS AND BIONICS and for the *International Journal of Humanoid Robotics*. He was an Associate Editor for the IEEE TRANSACTIONS ON ROBOTICS (2009–2013) and for *Soft Robotics* (2018–2021).

Dario Floreano (Senior Member, IEEE) received the M.A. degree in vision psychophysics, the M.S. degree in neural computation, and the Ph.D. degree in robotics.

He is currently a Full Professor and Director of the Laboratory of Intelligent Systems, Swiss Federal Institute of Technology Lausanne (EPFL), Lausanne, Switzerland. Since 2010, he is also a Founding Director of the Swiss National Center of Competence in Robotics. He held Visiting Fellowships with Sony Computer Science Laboratory, Tokyo, Japan, with Caltech/JPL, Pasadena, CA, USA, and with Harvard University in Boston, Boston, MA, USA. His research interests focus on biologically inspired robotics and artificial intelligence. He made pioneering contributions to the fields of evolutionary robotics, aerial robotics, and soft robotics. He spun off two robotics companies: senseFly (2009, acquired by the Parrot Group in 2016), which has become a world leader in drones for agriculture and imaging, and Flyability (2015), which is the world leader in inspection drones for confined spaces. In 2017, The Economist dedicated a center page portrait to Prof. Floreano (Brain Scan).

Prof. Floreano served in the Advisory Board of the Future and Emerging Technologies division of the European Commission, has been Vice-Chair of the World Economic Forum Agenda Council on Smart Systems and Robotics, has been a Cofounder of the International Society of Artificial Life, served as elected member of the Board of Governors of the International Neural Network Society, is on the Advisory Board of the Max-Planck Institute for Intelligent Systems, and has joined the editorial board of ten scientific journals. He also co-organized ten international conferences and several thematic workshops on bioinspired drones and soft robotics, which are now considered foundational events for those communities.